Protein-Cofactor Interactions in Bacterial Reaction Centers from *Rhodobacter sphaeroides* R-26: II. Geometry of the Hydrogen Bonds to the Primary Quinone $Q_A^{\cdot -}$ by ^1H and ^2H ENDOR Spectroscopy

M. Flores,*† R. Isaacson,* E. Abresch,* R. Calvo,*‡ W. Lubitz,† and G. Feher*

*Department of Physics, University of California at San Diego, La Jolla, California; †Max-Planck Institut für Bioanorganische Chemie, Mülheim an der Ruhr, Germany; and ‡Departamento de Física, Facultad de Bioquímica y Ciencias Biológicas and INTEC, Universidad Nacional del Litoral and CONICET, Santa Fe, Argentina

ABSTRACT The geometry of the hydrogen bonds to the two carbonyl oxygens of the semiquinone $Q_A^{\cdot -}$ in the reaction center (RC) from the photosynthetic purple bacterium *Rhodobacter sphaeroides* R-26 were determined by fitting a spin Hamiltonian to the data derived from ^1H and ^2H ENDOR spectroscopies at 35 GHz and 80 K. The experiments were performed on RCs in which the native Fe^{2+} (high spin) was replaced by diamagnetic Zn^{2+} to prevent spectral line broadening of the $Q_A^{\cdot -}$ due to magnetic coupling with the iron. The principal components of the hyperfine coupling and nuclear quadrupolar coupling tensors of the hydrogen-bonded protons (deuterons) and their principal directions with respect to the quinone axes were obtained by spectral simulations of ENDOR spectra at different magnetic fields on frozen solutions of deuterated $Q_A^{\cdot -}$ in H_2O buffer and protonated $Q_A^{\cdot -}$ in D_2O buffer. Hydrogen-bond lengths were obtained from the nuclear quadrupolar couplings. The two hydrogen bonds were found to be nonequivalent, having different directions and different bond lengths. The H-bond lengths $r_{O\cdots H}$ are 1.73 ± 0.03 Å and 1.60 ± 0.04 Å, from the carbonyl oxygens O_1 and O_4 to the NH group of Ala M260 and the imidazole nitrogen N_δ of His M219, respectively. The asymmetric hydrogen bonds of $Q_A^{\cdot -}$ affect the spin density distribution in the quinone radical and its electronic structure. It is proposed that the H-bonds play an important role in defining the physical properties of the primary quinone, which affect the electron transfer processes in the RC.

INTRODUCTION

Two ubiquinones, Q_A and Q_B, are present in the reaction centers (RCs) of photosynthetic purple bacteria and are actively involved in the coupled electron-proton transfer processes that lead to the formation of the proton gradient across the photosynthetic membrane required for ATP synthesis (1). The two quinones have different redox potentials providing the driving force for the vectorial electron transfer (ET) from the primary to the secondary quinone. Since Q_A and Q_B are chemically identical molecules, their different properties in the ET chain must result from specific interactions with the protein environment (2–6). One of these interactions is hydrogen bonding between the carbonyl oxygens of the quinones and the RC protein. Q_A forms two hydrogen bonds to the RC protein (2,3,7). The bonds contribute to the binding and to the unusual chemical properties and function of the quinone. It is, therefore, important to characterize them in detail.

X-ray crystallographic structures of proteins are usually not obtained at high enough resolution to provide direct information on the positions of protons (e.g., the protons hydrogen-bonded to the quinones). Furthermore, specific intermediate states of the reaction cycle (e.g., the semiquinone radical anions $Q_A^{\cdot -}$ and $Q_B^{\cdot -}$) are only accessible in exceptional cases by x-ray crystallography (e.g., (3,8)). Consequently, other methods have been used, in particular electron paramagnetic resonance (EPR) and electron nuclear double resonance (ENDOR) spectroscopies, to study semiquinone radicals in bacterial RCs (4–6,9–19). These spectroscopies provide information about the electronic and spatial structure of the transient radicals $Q_A^{\cdot -}$ and $Q_B^{\cdot -}$ (reviewed in (4–6)).

In this work we focus on the primary quinone Q_A, which accepts one electron to form the ubisemiquinone radical anion, $Q_A^{\cdot -}$. The experiments were performed on RCs in which the Fe^{2+} was replaced by Zn^{2+}. However, we expect our results to be valid for native RCs since all spectral and kinetic properties of Zn-RCs are identical to Fe-RCs (20,21). Details on the spin-density distribution of this species have been obtained earlier by EPR and ENDOR spectroscopy (9–18) and showed pronounced shifts of the hyperfine couplings of $Q_A^{\cdot -}$ when compared with the free $UQ_{10}^{\cdot -}$ radical anion in organic solvents. This effect has been attributed to asymmetric hydrogen bonding to $Q_A^{\cdot -}$ in the RC proteins (9,10). The hydrogen-bonded protons are exchangeable with deuterons (in D_2O buffer) and could thus be identified via $^1H \rightarrow {}^2H$ exchange experiments in the spectra.

In a previous article (19), the ENDOR lines belonging to the exchangeable protons have been assigned to two protons hydrogen-bonded to the two carbonyl oxygens of $Q_A^{\cdot -}$. In this work, we used ^1H- and ^2H-ENDOR spectroscopies to determine the geometry of the two hydrogen bonds. The ENDOR experiments were performed at 80 K and at a microwave frequency of 35 GHz (Q-band), which provides improved spectral resolution compared to the commonly used frequency of 9 GHz (X-band). This enabled us to select molecules with

Submitted June 29, 2006, and accepted for publication September 27, 2006.

Address reprint requests to G. Feher, Tel.: 858-534-4388; E-mail: gfeher@ucsd.edu.

0006-3495/07/01/671/12 $2.00

doi: 10.1529/biophysj.106.092460

particular sets of orientations with respect to the magnetic field (22). Since the ^{1}H and ^{2}H ENDOR spectra occur in different, nonoverlapping, frequency regions of the spectrum, we were able to simplify the ENDOR spectra (i.e., focus on the H-bonds) by using deuterated RCs in H_2O buffer and protonated RCs in D_2O buffer. Furthermore, the different $^1H \rightarrow {}^2H$ exchange rates of the two protons enabled us to preferentially deuterate (or protonate) one of the two carbonyl oxygens as described in (19). A standard spin Hamiltonian was fitted to the ENDOR spectra obtained at different magnetic field positions using the EasySpin package developed by Stoll and Schweiger (23). The fit yielded the principal components of the ^{1}H and ^{2}H hyperfine coupling (hfc) and the ^{2}H nuclear quadrupolar coupling (nqc) tensors and their principal directions with respect to the g-tensor axes of $Q_A^{\cdot -}$, which are related to the molecular axes of the quinone (13). The hydrogen-bond lengths were obtained from the ^{2}H nuclear quadrupolar couplings using the empirical relations of Soda and Chiba (24) and of Hunt and Mackay (25). By these procedures, the geometries of both hydrogen bonds were completely characterized.

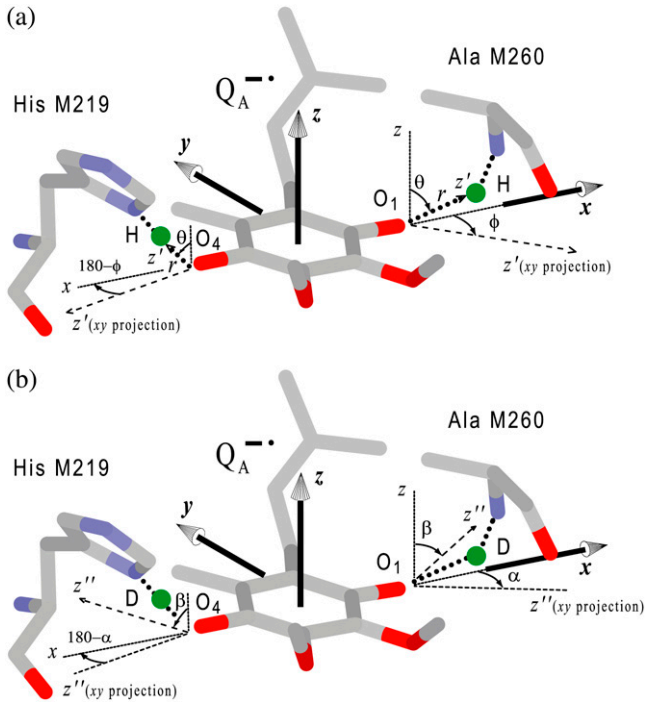

FIGURE 1 Structure in the vicinity of Q_A in the RC of *Rb. sphaeroides* (Brookhaven data bank entry 1AIG (3)) with the H-bonds (*a*), or the D-bonds (*b*) to the two carbonyl oxygens, O_1 and O_4. The principal axes of the g-tensor are along the molecular axes x, y, z (*a*). The principal axes of the hfc tensors of the protons in H-bonds are along the axes x', y', z' (for simplicity x' and y' are not shown, they lie in the plane perpendicular to z'), and are related to the g-tensor axes by the Euler angles ϕ and θ (31) (*a*). The proton in the hydrogen bond is characterized by the bond-length r and the angles θ and ϕ (*a*). The principal axes of the nqc tensor are along x'', y'', z'' (for simplicity x'' and y'' are not shown, they lie in the plane perpendicular to z''), and are related to the g-tensor axes by the Euler angles α, β and γ (31) (for simplicity γ is not shown) (*b*).

THEORY

Spin Hamiltonian and its relation to the structure

We focus on the interaction between the magnetic moment of the unpaired electron of $Q_A^{\cdot -}$ and the magnetic moments of protons or deuterons that form hydrogen bonds to the quinone oxygens O_1 and O_4 (see Fig. 1). The observed ENDOR spectra were interpreted using a spin Hamiltonian, $\mathcal{H}$, containing the electron and nuclear Zeeman interactions with the applied magnetic field $\mathbf{B_o}$, the hfc, and the nqc terms (e.g., (26)):

$$\mathcal{H} = \beta_e \mathbf{S}\cdot\mathbf{g}\cdot\mathbf{B_o} - \beta_N g_N \mathbf{I}\cdot\mathbf{B_o} + h\mathbf{S}\cdot\boldsymbol{A}\cdot\mathbf{I} + h\mathbf{I}\cdot\boldsymbol{P}\cdot\mathbf{I}, \quad (1)$$

where $\mathbf{S}$ is the electron spin operator, $\mathbf{I}$ is the nuclear spin operator of protons or deuterons in H-bonds to the carbonyl oxygens; $\boldsymbol{A}$ and $\boldsymbol{P}$ are the hfc and nqc tensors in frequency units, $\boldsymbol{g}$ is the electronic g-tensor, g_N is the g-factor of the corresponding magnetic nucleus (proton or deuteron) and β_e and β_N are the electron and nuclear magnetons, respectively, and h is Planck's constant. The first term in Eq. 1 represents the electronic Zeeman term that gives rise to the observed EPR spectra. The other three terms represent nuclear interactions, which are small and not resolved in the EPR spectrum but give rise to the ENDOR spectra. The hyperfine tensor component A_i is composed of anisotropic (dipolar) and isotropic contributions that can be written as

$$A_i = A_i' + A_{iso}. \quad (2)$$

For a proton in a typical hydrogen bond, the isotropic part A_{iso} is small compared to the anisotropic term A_i', which arises from the dipolar interaction between the unpaired electron and the proton. In the simple point-dipole approximation (e.g., (26)) the anisotropic term can be written as

$$A_i'(\delta) = \frac{g_e\beta_e g_N\beta_N}{hr^3}\rho(3\cos^2\delta - 1) = \frac{79.2}{r^3}\rho(3\cos^2\delta - 1)[\mathrm{MHz}], \quad (3)$$

where g_e and g_N are the electron and proton g-values, ρ is the unpaired electron spin density at the quinone oxygen, δ is the angle between the applied magnetic field and the direction of the hydrogen bond, and r is the H-bond length in Å (for deuterons the numerical factor 79.2 is replaced by 12.16). The traceless tensor resulting from this approximation is axially symmetric, with principal components $A_\parallel'$ for $\delta = 0°$ (direction along the hydrogen bond) and $A_\perp'$ for $\delta = 90°$, with $A_\parallel' = -2\,A_\perp'$. The point-dipole model for the hyperfine interaction of H-bonds (see Eq. 3) has been shown to be valid in good approximation for quinone model compounds (27,28), in which the H-bonds lie in the quinone plane. In RCs, this is not the case leading to the difficulties discussed in the section on the H-bond lengths.

For nuclei with $I \geq 1$, the nuclear quadrupolar interaction is described by a traceless tensor with principal components P_i (i = 1,2,3) with $|P_1| \geq |P_2| \geq |P_3|$. It has been shown (24,29,30) that the largest component P_1 is approximately along the direction of the H-bond, P_2 is parallel to the normal of the plane of the hydrogen-bond donor molecule, and P_3 is perpendicular to the directions of P_1 and P_2. The principal values P_i can be obtained from single crystal or, as has been done in this work, from orientationally selected ENDOR spectra. It is customary to describe the nqc tensor by the nuclear quadrupole coupling e^2qQ/h (in frequency units) and an asymmetry parameter η (e.g., (26)) as

$$e^2qQ/h = eQV_1/h = 2P_1 \tag{4}$$

and

$$\eta = |(V_3 - V_2)/V_1|, \tag{5}$$

where Q is the scalar nuclear quadrupole moment ($Q_{2_H} = +2.74 \times 10^{-27}$ cm^2), e the electronic charge, the V_i values are the principal values of the electric field gradient tensor $V_{ij} = \partial^2 V/(\partial x_i \partial x_j)$, where x_i and x_j are the nuclear coordinates and V is the electrostatic potential. The parameter η describes the deviation from axial symmetry of the quadrupolar tensor, i.e., of the electric field gradient. The field gradient V_{ij} is related to the distribution of electrical charges around the nucleus and thus to the specific bonding geometry. Its value can, therefore, be used to obtain information on the hydrogen bonds (24,25,27–30).

Molecular structure and axis system

Since the hfc and nqc tensor axes are not collinear with the g-tensor axes of the semiquinone (27,28), we describe these tensors by their principal components and the Euler angles (31) relating their principal axes to the g-tensor axes (see Fig. 1). Furthermore, the hfc tensor of the H-bond is expected to have nearly axial symmetry (27,28). Therefore, its axes with respect to the g-tensor axes can be determined by only the two Euler angles defining the axial direction, which corresponds to the largest component of the hfc tensor (see Eq. 3).

In this work, we used samples frozen at 80 K containing randomly oriented molecules. ENDOR spectra were obtained at different magnetic fields within the EPR spectrum, along which molecules with a particular set of directions were selected (22,31–33). The orientation selection is produced by the anisotropy of the electronic g-tensor. The global analysis by computer simulations of the ENDOR spectra (e.g., (32,33)), using the spin Hamiltonian of Eq. 1, yielded both the principal components of the hyperfine and quadrupolar coupling tensors, and their orientation (i.e., Euler angles) with respect to the principal axes x, y, z of the g-tensor of $Q_A^{\cdot -}$, whose orientation with respect to the molecular axes is known from EPR experiments performed in single crystals of RCs (13) (see Fig. 1).

The $Q_A^{\cdot -}$ molecule with two H- or D-bonds from the carbonyl oxygens to the imidazole nitrogen of His (M219) ($N_\delta - H^{\cdot\cdot} O_4$) and to the NH group of Ala (M260) ($N - H^{\cdot\cdot} O_1$) are shown in Fig. 1, *a* and *b*, respectively. The principal axes of the g-tensor are parallel to the molecular axes x, y, z, with the z-axis perpendicular to the π-plane (13). The principal axes of the hfc tensor of the hydrogen bonds H or D are denoted by x', y', z' (for simplicity x' and y' are omitted in Fig. 1 *a*) and those of the nqc tensor by x'', y'', z'' (for simplicity x'' and y'' are omitted in Fig. 1 *b*), with z' and z'' (axes defined by the two first Euler rotations) corresponding to the largest components of the hfc and nqc tensors, respectively. Fig. 1, *a* and *b*, also show the Euler angles (ϕ, θ) and (α, β) relating the x', y', z' and x'', y'', z'' axes to the g-tensor axes (31) (for simplicity γ is omitted). Note that for the hfc tensor, only two Euler angles are needed. Our goal is to determine the geometry of the H-bonds (i.e., r, θ, and ϕ) from the values of the principal components of the hfc and nqc tensors and their respective Euler angles.

MATERIALS AND METHODS

Sample preparation and nomenclature

The preparation and deuteration of the reaction centers, the proton-deuterium exchange, and the generation of the semiquinone radical anion have been described in a previous article (19). The paramagnetic nonheme Fe^{2+} was chemically removed and replaced with diamagnetic Zn^{2+} to reduce the EPR line width of the semiquinone, following the procedure of Utschig et al. (21). The ratio of Zn/RC was determined by atomic absorption spectroscopy and Q-band EPR spectroscopy to be $\geq$0.90. Since we used several combinations of protonated and deuterated RCs and buffer, we define the following notation: $pQ_A^{\cdot -}$ for $Q_A^{\cdot -}$ in fully protonated RCs, $dQ_A^{\cdot -}$ for $Q_A^{\cdot -}$ in fully deuterated RCs, and H_2O for fully protonated and D_2O for fully deuterated buffer.

EPR and ENDOR instrumentation

EPR and ENDOR measurements were performed at 35 GHz (Q-band) and 80 K. The Q-band spectrometer has been previously described (19). ENDOR experiments were performed with the EPR spectra 50% saturated. ENDOR spectra were recorded for different settings of the magnetic field within the EPR spectrum (12 positions for protons and 11 positions for deuterons), using frequency modulation (FM) of $\pm$140 kHz for protons and $\pm$30 kHz for deuterons. The output of the RF amplifier (ENI 3100L) feeding the ENDOR coils was 50 W for protons and 25 W for deuterons. To improve the signal-to-noise ratio many ENDOR traces were averaged.

RESULTS AND DISCUSSION

EPR experiments

The Q-band EPR spectrum of $Q_A^{\cdot -}$ at T = 80 K in deuterated RCs and protonated buffer ($dQ_A^{\cdot -}$ in H_2O) is shown as a solid line in Fig. 2 *a* and the spectrum in protonated RCs and deuterated buffer ($pQ_A^{\cdot -}$ in D_2O) in Fig. 2 *b*. For $dQ_A^{\cdot -}$ in H_2O (Fig. 2 *a*), the broadening of the spectrum is mainly due to hyperfine interactions of protons in solution (exchangeable protons), including the H-bonds to the carbonyl oxygens. For

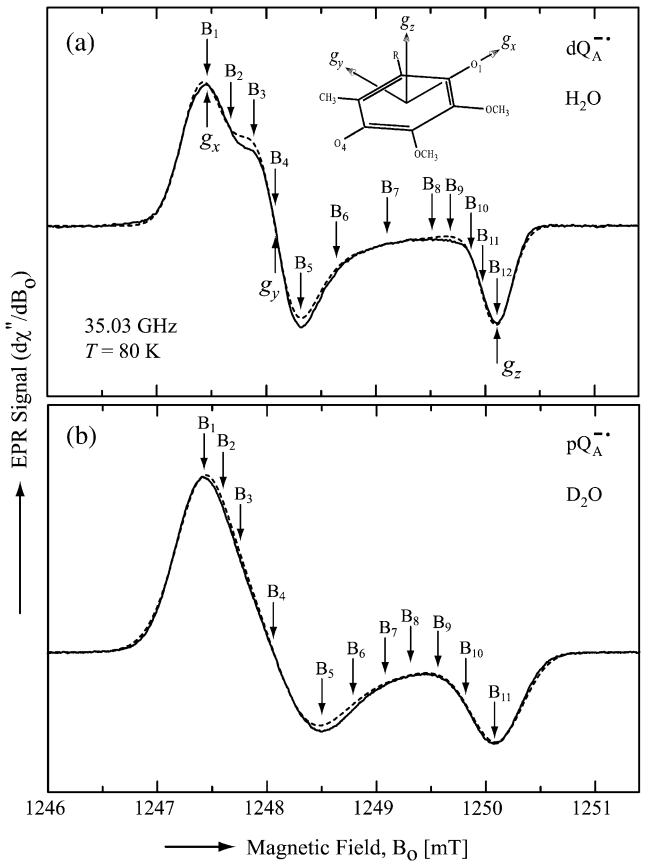

FIGURE 2 EPR powder spectra of $dQ_A^{\cdot-}$ in H_2O (*solid lines*) (*a*) and $pQ_A^{\cdot-}$ in D_2O (*solid lines*) (*b*). ENDOR spectra were taken at the field positions indicated by arrows. The inset shows the principal axes of the *g*-tensor of the ubisemiquinone. The simulated spectra are shown by dashed lines. The linewidth values of ΔB_x, ΔB_y, and ΔB_z obtained from the simulation are 0.45 mT, 0.34 mT, and 0.16 mT, respectively, for $dQ_A^{\cdot-}$ in H_2O (*a*) and 0.47 mT, 0.64 mT, and 0.47 mT, respectively, for $pQ_A^{\cdot-}$ in D_2O (*b*). Experimental conditions: $T =$ 80 K, microwave (MW) frequency = 35.03 GHz, MW power = 1×10^{-7} W (*a*) and 3×10^{-7} W (*b*); field modulation = 0.15 mT peak-to-peak at 270 Hz, average of nine scans (*a*) and of four scans (*b*), 20 s per scan.

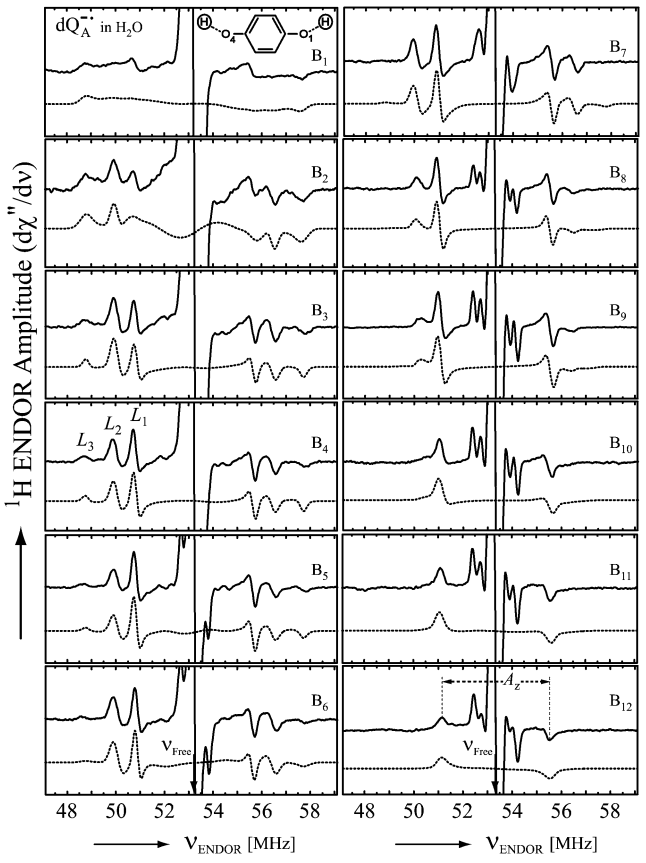

FIGURE 3 Experimental (*solid lines*) and simulated (*dotted lines*) ^{1}H ENDOR spectra of $dQ_A^{\cdot-}$ in H_2O, at 35 GHz, at 12 different magnetic field positions of the EPR spectrum (see *arrows* in Fig. 2 *a*). In the fitting of the spin Hamiltonian to the data the frequency range between 51.5 MHz and 55.0 MHz was excluded. The H-bond ENDOR lines L_1, L_2, L_3 are labeled in (B_4). The hfc splitting A_z is shown by an arrow in (B_{12}). Experimental conditions: $T =$ 80 K, MW power = 3×10^{-6} W, and frequency modulation (FM) = $\pm$140 kHz at a rate of 947 Hz. Number of scans per position: 600. Scan time: 4 s.

$pQ_A^{\cdot-}$ in D_2O (Fig. 2 *b*), the broadening is mainly due to the hyperfine interactions of quinone protons (methyl, methoxy, and methylene protons) and those associated with the protein in the vicinity of the binding site. To obtain molecular orientation selection, ENDOR spectra were recorded at the magnetic field positions indicated by arrows in Fig. 2, *a* and *b* (magnetic field positions corresponding to the principal directions of the *g*-tensor are also given in Fig. 2 *a*).

ENDOR experiments

Fig. 3 shows the experimental Q-band ^{1}H ENDOR spectra (*solid lines*) of $dQ_A^{\cdot-}$ in H_2O, arising from the two ^{1}H-bonds (at frequencies $<$51.5 MHz and $>$55.0 MHz) and from exchangeable protons belonging to other residues in the neighborhood of $Q_A^{\cdot-}$ (in the frequency region between 51.5 MHz and 55.0 MHz). At the magnetic field positions from B_1 (g_x) to B_6 (Fig. 3) the spectra correspond to a two-dimensional powder-type spectrum with weighted contributions mainly from molecules that have the magnetic field pointing in the plane of the quinone (referred to as in-plane directions). Therefore, a powder spectrum with two sharp features, corresponding approximately to the $A_{x'}$ and $A_{y'}$ components of the hfc tensor is observed for each H-bond. The lines associated with the H-bonds are labeled L_1, L_2, and L_3 in Fig. 3, B_4 (g_y). The splittings observed at g_y are similar to those previously observed at X-band (6). These ENDOR lines were recently identified by selectively deuterating one of the H-bonds to the quinone (19). It was shown that the peaks L_1 and L_2 are associated with two different protons and that the peak L_3 is an overlap of two lines, one being a partner of L_1 and the other of L_2.

At higher magnetic field positions (Fig. 3, B_7–B_{12}), the ENDOR spectra arise mainly from the weighted contributions from molecules that have the magnetic field pointing out of the plane of the quinone (referred to as out-plane directions),

and contain one sharp feature for each H-bond tensor. The lines corresponding to the ^{1}H-bonds are centered around the ^{1}H Larmor frequency (53.3 MHz at B_{12}) and are split by their respective A_z values (Fig. 3, B_{12}). At B_{12} (g_z) (Fig. 3) the lines corresponding to the two H-bonds overlap.

Fig. 4 shows the ^{2}H ENDOR spectra (*solid lines*) of $pQ_A^{\cdot -}$ observed after preparing the RCs in H_2O and incubating them for 50 min in D_2O. Under these conditions, the hydrogen bond to O_1 (see Fig. 1) is preferentially deuterated, as described in Flores et al. (19). Thus, the observed lines arise from the D-bond to O_1 (see *inset* in Fig. 4) and from other exchangeable deuterons (see also Fig. 5). At the magnetic field positions from B_1 to B_9 (see *arrows* in Fig. 2 *b*), a two-dimensional powder-type spectrum, analogous to Fig. 3, is obtained. At B_{11} a single-crystal like spectrum with two doublets centered around the ^{2}H Larmor frequency (8.18 MHz) is observed. The splitting of the doublets is given approximately by the quadrupolar interaction $3P_z$; the splitting between the centers of the doublets is $\sim A_z$.

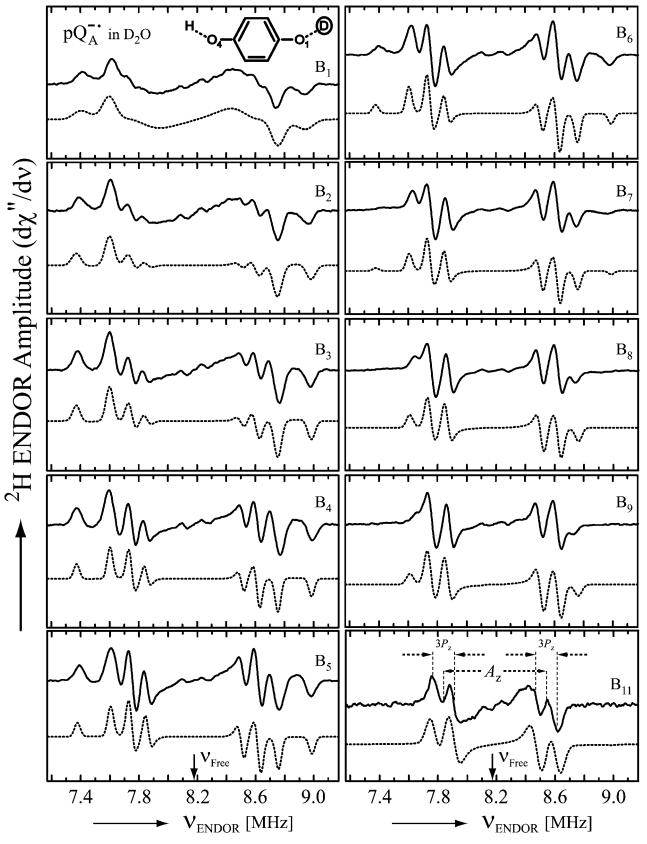

FIGURE 4 Experimental (*solid lines*) and simulated (*dotted lines*) ^{2}H ENDOR spectra of $pQ_A^{\cdot -}$ at 35 GHz in RCs prepared in H_2O and incubated for 50 min in D_2O (see (19)), at 10 different magnetic field positions of the EPR spectrum (see *arrows* in Fig. 2 *b*). Inset shows the preferential deuteration of the bond to O_1. The quadrupolar splittings $3P_z$ and hyperfine splitting A_z are shown by arrows in the single-crystal-type spectrum at position B_{11}. Experimental conditions: $T = 80$ K, MW power $= \sim 5 \times 10^{-6}$ W, and FM $= \pm 30$ kHz at a rate of 985 Hz. Number of scans per position: 45,000. Scan time: 4 s.

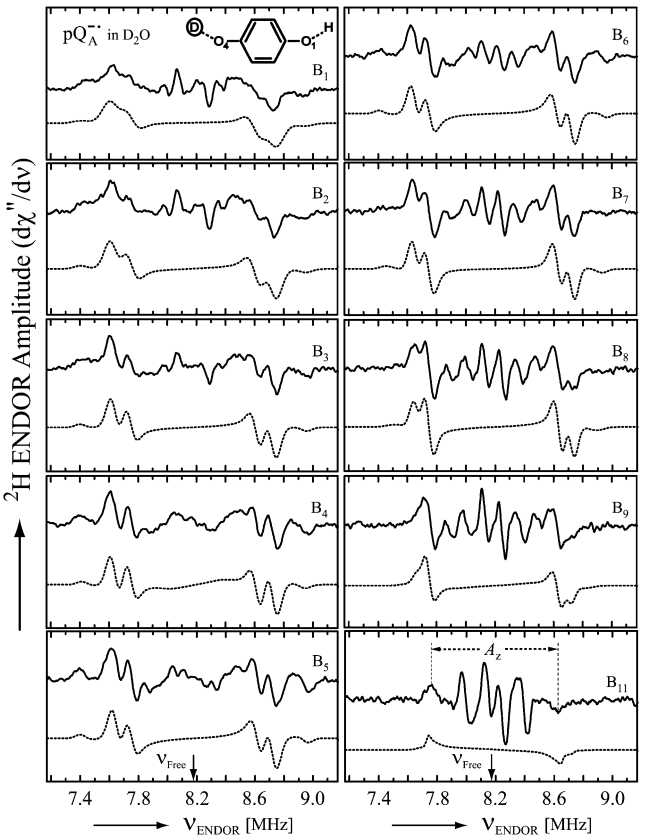

FIGURE 5 Experimental (*solid lines*) and simulated (*dotted lines*) ^{2}H ENDOR spectra of $pQ_A^{\cdot -}$ at 35 GHz in RCs prepared in D_2O and incubated for 190 min in H_2O (see (19)), at 10 different magnetic field positions of the EPR spectrum (*see arrows* in Fig. 2 *b*). Inset shows the preferential deuteration of the bond to O_4. The hyperfine splitting A_z is shown by an arrow in the single-crystal-type spectrum at position B_{11}. Experimental conditions: $T = 80$ K, MW power $= \sim 5 \times 10^{-6}$ W, FM $= \pm 30$ kHz at a rate of 985 Hz. Number of scans per position: 70,000. Scan time: 4 s.

Fig. 5 shows the ^{2}H ENDOR spectra (*solid lines*) of $pQ_A^{\cdot -}$ observed after preparing the RCs in D_2O and incubating them for 190 min in H_2O. Under these conditions, the hydrogen bond to O_4 (see Fig. 1) is preferentially deuterated (19) (see *inset* in Fig. 5). ^{2}H ENDOR lines observed at frequencies <7.8 MHz and >8.5 MHz correspond to the D-bond to O_4. ^{2}H ENDOR lines observed in the region between 7.8 MHz and 8.5 MHz correspond to exchangeable deuterons from residues in the neighborhood of $Q_A^{\cdot -}$ (e.g., Trp M252 and Thr M222). The lines corresponding to the D-bond to O_4 show a two-dimensional powder pattern from B_1 to B_9 (Fig. 5) as in Fig. 4. At B_{11} (g_z) the nqc splitting becomes small and only the hfc splitting is observed.

Analysis of the data

Numerical fitting procedures

To compare experimental and simulated EPR and ENDOR spectra, we divided the spectra into N intervals, i.e., we

treated the spectrum as an N-dimensional vector $\mathbf{R}$. Each component R_j has the amplitude of the signal at a frequency ν_j, with j varying from 1 to N. The amplitudes of the experimental and simulated spectra were normalized so that the span between the maximum and minimum values of R_j is 1. We compared the calculated amplitudes R_j^{calc} of the signal with the observed values R_j defining a root mean-square deviation σ by

$$\sigma(p_1,p_2,\ldots,p_n)=[\sum_j(R_j^{calc}(p_1,p_2,..,p_n)-R_j^{exp})^2/N]^{1/2}, \quad (6)$$

where the sums are over the N values of j, and p-values are the fitting parameters that produced the calculated spectrum. For the simulation of the EPR spectra $N = 1024$ and of the ENDOR spectra $N = 667$.

The EPR spectra were fitted with the program SAFIT, which we had developed earlier for randomly oriented radicals (powder samples) (34). The program is based on the simulated annealing method (35) and uses a Monte Carlo type iteration to minimize the root mean-square deviation, σ (see Eq. 6), between measured and simulated spectra. We searched for the optimum values of the parameters g_x, g_y, and g_z and the line-widths ΔB_x, ΔB_y, and ΔB_z.

For the ENDOR spectra, we defined a global root mean-square deviation σ_G by

$$\sigma_G=[\sum_k(\sigma_k)^2]^{1/2}, \quad (7)$$

where σ_k is the root mean-square deviation (given by Eq. 6) corresponding to the ENDOR spectrum at the magnetic field position B_k. For the ^{1}H ENDOR spectra $k = 1,\ldots,12$ and for ^{2}H ENDOR spectra $k = 1,\ldots,11$.

The ENDOR spectra were simulated using EasySpin, a computational package developed by Stoll and Schweiger (23) and based on Matlab (The MathWorks, Natick, MA). EasySpin calculates ENDOR frequencies using the energies of the states of the spin system obtained by direct diagonalization of the spin Hamiltonian (see Eq. 1). Two sets of parameters were used in the simulations. The first set includes the EPR parameters, i.e., the microwave frequency, g-factors (obtained from the fitting of the EPR line) and magnetic field position. These parameters remained fixed in the ENDOR simulations. The second set consists of the following fitting parameters: the principal values and Euler angles of the hyperfine interaction ($A_{x'}$, $A_{y'}$, $A_{z'}$, ϕ, θ) and nuclear quadrupolar ($P_{x''}$, $P_{y''}$, $-P_{x''}-P_{y''}$, α, β, γ) tensors, the excitation width (Δw_k) (i.e., the EPR line-width at the magnetic field position of the ENDOR measurement), and the ENDOR line-width ($\Delta\nu_k$). These parameters were varied iteratively, one at a time, to simultaneously optimize the fit of the ENDOR spectra at different positions of the EPR spectrum by minimizing the value of σ_G (Eq. 7, global fitting). Typical values of σ_G were between 3% and 8%, with the lowest values corresponding to the ^{1}H ENDOR spectra. The process was terminated when no further changes in the values of the fitting parameters were observed. This required typically between 6 and 10 iterations over the full set of fitting parameters.

^{1}H ENDOR spectra corresponding to each H-bond were not obtained separately, due to the short $^1H \rightarrow {}^2H$ exchange time of the H-bond to Ala (M260) in deuterated RCs (see Fig. 4 *a* in reference 19). Preparing a high concentration sample takes at least 25 min (see (19), Materials and Methods). Therefore, we fitted the ^{1}H ENDOR spectra that contain the lines associated with the two H-bonds (see Fig. 3). Thus, two spectra were calculated simultaneously, one corresponding to $N-H\cdots O_1$ (Ala M260) and the other one corresponding to $N_\delta-H\cdots O_4$ (His M219) taking into account the overlap observed at L_3. Consequently, σ and σ_G were calculated for the sum of these two spectra. Because of the interfering ^{1}H ENDOR lines from other exchangeable protons, the region of the spectrum between 51.5 MHz and 55.0 MHz was excluded from the calculation of σ and σ_G. However, the ^{2}H ENDOR spectra corresponding to each D-bond, i.e., $N-D\cdots O_1$ (Ala M260, see Fig. 4) or $N_\delta-D\cdots O_4$ (His M219, see Fig. 5), were obtained separately due to the longer $^1H \rightarrow {}^2H$ exchange times observed in protonated RCs (see Fig. 4 *b* in reference 19). Therefore, the ^{2}H ENDOR spectra of each D-bond were fitted independently. To avoid interfering ^{2}H ENDOR lines from other exchangeable deuterons, the region between 7.8 MHz and 8.5 MHz was excluded from the simulation of the spectra corresponding to $N_\delta-D\cdots O_4$ (see Fig. 5).

Spin Hamiltonian parameters obtained from the fit of the spectra

The fit of the EPR spectra is shown by dotted lines in Fig. 2. The values of g_x, g_y, and g_z were obtained from the fitting and are summarized in Table 1. These values are in agreement with those reported previously (13,36). The principal axes of the g-tensor are along the quinone axes xyz (13) (see *inset* in Fig. 2), providing a convenient reference system for describing the geometry of the hydrogen bonds (see Fig. 1). The values of ΔB_x, ΔB_y, and ΔB_z obtained from the fitting are given in the caption of Fig. 2. However, these values are not used in the simulation of the ENDOR spectra (see previous section).

The principal components of the hfc tensor $\boldsymbol{A}$ and the Euler angles, ϕ (in-plane angle) and θ (*azimuthal* angle), associated with rotations of the principal axes $x'y'z'$ with respect to the g-tensor axes xyz (see Fig. 1 *a*), were obtained from the global fitting of the ^{1}H ENDOR spectra of $dQ_A^{\cdot-}$ in H_2O (see Fig. 3). As explained before, only two Euler angles are relevant as a consequence of the nearly axial symmetry of the hfc tensor (the deviation from axial symmetry is ~8% for $N-H\cdots O_1$ and ~0.3% for $N_\delta-H\cdots O_4$; see Table 1). They determine the direction of z' with respect to the xyz axes. The values obtained at the minimum σ_G are summarized in Table 1. The hfc values are in agreement with earlier, less accurate, ^{1}H ENDOR experiments (6,10). The signs of the ^{1}H hfc

TABLE 1 Parameters used in the fittings of ENDOR spectra of $dQ_A^{\cdot -}$ in H_2O and $pQ_A^{\cdot -}$ in D_2O at 35 GHz and $T = 80$ K

Direction	x	y	z
g-value (± 0.0001)	2.0065	2.0053	2.0021
Hyperfine components (A_i)	$A_{x'}$ [MHz]	$A_{y'}$ [MHz]	$A_{z'}$ [MHz]
N−H···O_1 (Ala M260)	−4.54 ± 0.02	−4.93 ± 0.02	+8.95 ± 0.07
N−D···O_1 (Ala M260)	−0.70 ± 0.01	−0.76 ± 0.01	+1.37 ± 0.02
N_δ−H···O_4 (His M219)	−6.49 ± 0.03	−6.51 ± 0.02	+9.15 ± 0.10
N_δ−D···O_4 (His M219)	−0.98 ± 0.01	−1.00 ± 0.01	+1.36 ± 0.03
Euler angles (between $\boldsymbol{A}$ and $\boldsymbol{g}$) [deg]	ϕ	θ	
N−H···O_1 (Ala M260)	−16 ± 8	63 ± 2	
N−D···O_1 (Ala M260)	−14 ± 8	68 ± 3	
N_δ−H···O_4 (His M219)	−167 ± 2	50 ± 2	
N_δ−D···O_4 (His M219)	−160 ± 6	54 ± 2	
Quadrupolar components ($2P_i$)	$2P_{x''}$ [kHz]	$2P_{y''}$ [kHz]	$2P_{z''}$ [kHz]
N−D···O_1 (Ala M260)	−140 ± 10	−62 ± 6	+202 ± 6
N_δ−D···O_4 (His M219)	−82 ± 6	−86 ± 8	+168 ± 10
Euler angles (between $\boldsymbol{P}$ and $\boldsymbol{g}$) [deg]	α	β	γ
N−D···O_1 (Ala M260)	−17 ± 10	47 ± 3	10 ± 10
N_δ−D···O_4 (His M219)	−175 ± 8	37 ± 3	−*

*The nqc tensor corresponding to N_δ−D···O_4 has axial symmetry, so its axes with respect to the g-tensor are determined by only two Euler angles (α and β).

values were deduced from theoretical considerations assuming that the largest anisotropic tensor component is positive, which also follows from the dipolar model and is in agreement with molecular orbital calculations (28,37). Since we are working with samples containing randomly oriented molecules, multiple (eight) solutions were obtained for the orientation (ϕ and θ) of the hfc tensor. Fig. 1 *a* shows one of the eight possible solutions for each H-bond. The other solutions are those obtained by reflections on the planes *xy*, *yz*, and *zx*. EPR and ENDOR cannot, in principle, distinguish between these solutions. To select the correct solution for the orientations of the hfc and nqc tensors we compared our results with structural data derived from x-ray crystallography on the RC ground state (see below). This approach assumes that the position of the quinone does not change significantly in the relaxed, charge separated state (8). The data provide a crude structural guideline, which is, however, sufficient to select the right solution (see section on the geometry of the H-bonds to Q_A).

The values of θ indicate that both hydrogen bonds lie out of the quinone plane (see Fig. 1 *a*). Furthermore, both H-bonds deviate by $\phi \approx 15°$ from the C−O bond direction (projection on the plane of the quinone) (see Fig. 1 *a*). This situation is different from that observed for the benzosemiquinone radical anion in water (27,28), in which the H-bonds lie in the quinone plane and approximately along the direction of the lone pair orbital of the oxygen ($\phi \approx 36°$). The uncertainties of the values of the fitting parameters (see Table 1) were estimated from the sensitivities of σ_G to these parameters (as discussed in (27); see Fig. 6 in that article). The simulated spectra calculated with the optimum values of the parameters are shown in Fig. 3 (*dotted lines*).

The principal components of the nqc tensor $\boldsymbol{P}$ and the Euler angles, α, β, and γ, associated with rotations of the x'', y'', z'' axes with respect to the g-tensor axes, *x, y, z* (see Fig. 1 *b*), were obtained from the fitting of the ^{2}H ENDOR spectra (see Figs. 4 and 5). The principal components of the ^{2}H nqc and ^{2}H hfc tensors, and the values of the Euler angles (α, β, γ) and (ϕ, θ) are summarized in Table 1. The correct set of values of α, β, and γ was selected by comparison with the x-ray crystallographic structure of the RC, as described above. The signs of the $P_{i''}$ components were determined from the following consideration: For the vast majority of hydrogen bonds the largest principal component of the ^{2}H nqc is positive (24,30,38,39), which is also supported by recent DFT calculations (28). A negative sign has only been proposed for extremely short H-bonds (39). Thus, the positive sign chosen for the larger principal component (Table 1) can safely be assumed to be correct for both ^{2}H nqc tensors. The quadrupole coupling constants (see Eq. 4 and Table 1) and in particular the asymmetry parameters (using Eq. 5, a value of $\eta = 0.39$ and $\eta = 0.02$ is obtained for Ala M260 and His M219, respectively) are quite different for the two hydrogen bonds, indicating different strengths and geometries of the two bonds (see below). The values of θ and ϕ obtained from the ^{2}H ENDOR spectra are, within experimental error, in agreement with those obtained from the fitting of the ^{1}H ENDOR spectra (see Table 1). The simulated spectra calculated with the optimum values of the parameters are shown in Figs. 4 and 5 (*dotted lines*); the agreement with the experimental spectra is very satisfying.

Geometry of the H-bonds to Q_A inferred from the x-ray structure

The occurrence of several (eight) numerical solutions for ϕ and θ described in the previous section is a general problem that occurs in magnetic resonance experiments on powder samples containing randomly oriented molecules. This problem has not been well discussed in previous ENDOR studies. The occurrence of several solutions is due to the invariance of the simulated ENDOR spectra under reflections of the proton position on the planes *xy*, *yz*, *zx* (see Fig. 1). Thus, the eight solutions are mathematically equivalent (symmetry-related) but differ in geometry. To solve this problem, we estimated values for ϕ and θ using the x-ray structure of the RC. Although these values are taken from the RC ground (dark) state and are not very precise due to the limited resolution of the crystals, they are sufficiently accurate to select the correct solution for our problem. This assumes that the charge separated and non-charge-separated structures do not differ significantly. This has been shown to be the case for Q_A and $Q_A^{\cdot -}$ by Abresch et al (8).

We inferred the geometry of the H-bonds to Q_A from the x-ray structure using the following procedure:

1. The protons in hydrogen bonds were placed in the structure at ideal positions determined geometrically by the theoretical values of the N−H bond length (1.0 Å) and the C−N−H angle (120° for Ala M260 and 126° for His M219), with the protons located in the plane of the C−N−C bond (from the backbone for Ala M260 and from the aromatic ring for His M219).
2. To model the deviations from the ideal positions, due to interactions with the surroundings (e.g., with the quinone), the positions of the protons were optimized by minimizing their van der Waals energies.
3. The hydrogen-bond lengths (r) and directions (ϕ and θ) were calculated using the coordinates of the quinone and the optimized coordinates of the protons; r is the distance between O and H, θ is the angle between the vector along the H-bond and the molecular z axis of the quinone, and ϕ is the angle between the projection of the H-bond onto the quinone plane and the x axis (see Fig. 1).

The first two steps (1 and 2) were done using the program CNS_Solve (40) and the last step (3) using a routine written in Matlab. This procedure was applied to nine x-ray structures from RCs of *Rb. sphaeroides* (PDB entries: 1AIG, 1AIJ (3); 1DS8, 1DV3, 1DV6 (41); 1L9B, 1L9J (42); 1OGV (7); and 1PCR (2)). The values of r, ϕ, and θ obtained from the structures (see Supplementary Material) do not show large deviations, indicating that the x-ray structures used in this work are reliable and represent a statistical collection of similar crystals. Thus, the mean values and standard deviations of the lengths and directions of the H-bonds to Q_A were calculated and are summarized as follows:

$$r_{O1\cdots H} = 2.05 \pm 0.13 \text{Å}, \quad \phi = -32° \pm 7°, \theta = 60° \pm 7° (\text{Ala M260}) \tag{8}$$

$$r_{O4\cdots H} = 1.90 \pm 0.13 \text{Å}, \quad \phi = -173° \pm 10°, \theta = 39° \pm 9° (\text{His M219}). \tag{9}$$

The geometry of the H-bonds to Q_A obtained here (Eqs. 8 and 9) was used to select the right solution out of the eight possible ones obtained experimentally for $Q_A^{\cdot -}$. Thus, the correct values for ϕ and θ obtained from the ENDOR analysis are those in Table 1 (see also Fig. 1).

The lengths of the H-bonds to $Q_A^{\cdot -}$ are expected to be shorter than those to Q_A, since the C−O bond lengths in the semiquinone radical anion are larger than in the quinone and the negative partial charge on the carbonyl oxygens in $Q_A^{\cdot -}$ attracts the proton and leads to a shortening of the H-bond. A different approach to obtain the geometry of the H-bonds to Q_A is to perform a geometry optimization within the framework of density functional theory. Such an approach is described in Sinnecker et al. (43).

Directions of the H-bonds to $Q_A^{\cdot -}$

The fitting of the ENDOR spectra (see Figs. 3–5), modeled by the spin Hamiltonian of Eq. 1, yielded the principal components of the hyperfine and quadrupolar coupling tensors corresponding to the two protons or deuterons hydrogen bonded to $Q_A^{\cdot -}$, as well as their orientation with respect to the principal axes xyz of the g-tensor which are equivalent to the molecular axes of the quinone (see Table 1 and Fig. 1). This determines the directions of the hydrogen bonds to the two carbonyl oxygens of $Q_A^{\cdot -}$. Two different H-bond directions were obtained. The H-bond to His (M219) is oriented out of the quinone plane by ~40°, whereas the one to Ala (M260) is ~27° out of the plane. Both are not oriented along the lone pair direction at the oxygen (judged from the in-plane angle ϕ, see Fig. 1). Strong hydrogen bonds are in general linear (44), i.e., the N−H···O angle is close to 180° with the proton located in the plane of the C−N−C bond structure (backbone of Ala or ring plane of His). This condition is closely fulfilled for the H-bond to His (M219) (160° ± 9°, obtained from the analysis described in the previous section) but not for the one to the N−H backbone of Ala (M260), where the respective angle is 133° ± 10°. This is clearly evident from Fig. 1. This geometrical situation found for the two hydrogen bonds to $Q_A^{\cdot -}$ indicates that the one to Ala (M260) is probably weaker than the one to His (M219) (see Table 2 in reference 45). This idea is supported by the fact that the length of the H-bond is shorter to His (M219) than to Ala (M60) (see below).

To fully characterize the H-bond geometry we also need to determine the bond lengths. These values can, in principle, be obtained either from the ^{1}H or ^{2}H dipolar coupling (Eq. 3) or from the ^{2}H nuclear quadrupolar couplings as discussed in the next two sections.

H-bond lengths calculated from the dipolar hyperfine couplings

The point-dipole model (Eq. 3) has been shown to be applicable to quinone model compounds in which the H-bonds lie in the quinone plane (27,28). In this geometrical situation

TABLE 2 Dipolar (A_i') and isotropic (A_{iso}) hyperfine couplings corresponding to protons and deuterons in hydrogen bonds to $Q_A^{\cdot -}$

	O_1–Ala (M260)		O_4–His (M219)	
	^{1}H	^{2}H × 6.514*	^{1}H	^{2}H × 6.514*
$A_{z'}'$ [MHz]	+9.12 ± 0.08	+9.12 ± 0.05	+10.43 ± 0.11	+10.23 ± 0.08
$A_{y'}'$	−4.75 ± 0.04	−4.76 ± 0.03	−5.23 ± 0.04	−5.15 ± 0.03
$A_{x'}'$	−4.37 ± 0.04	−4.36 ± 0.03	−5.20 ± 0.05	−5.08 ± 0.03
A_{iso}	−0.17 ± 0.03	−0.20 ± 0.03	−1.28 ± 0.04	−1.37 ± 0.03

Values were calculated using the ^{1}H and ^{2}H hfc tensor components in Table 1 and Eq. 2 (see Discussion).

*To compare the proton and deuteron HFCs, the ^{2}H results were multiplied by $\gamma_{1_H}/\gamma_{2_H} = 6.514$.

the effective overlap of the hydrogen 1s orbital with the π-orbital at the oxygen is small and the point-dipole approximation is valid for distances $\geq$2.0 Å (28). However, in RCs the H-bond is up to 40° out of the quinone plane (Table 1). This results in an additional interaction between the proton and the π-orbital of the oxygen. This increased interaction effectively leads to a smaller (and erroneous) bond length when Eq. 3 is used (28). An additional disadvantage of the application of the point-dipole model is that the spin density at the contact position (here the carbonyl oxygens) must be known. For $Q_A^{\cdot -}$ this has been determined by EPR performed on ^{17}O-labeled $Q_A^{\cdot -}$ (6,9,10). Using spin densities at the quinone oxygens, of $\rho(O_1) = 0.21$ and $\rho(O_4) = 0.15$ (6,10), Eq. 3 yields bond lengths of $r_{O_1\cdots H} = 1.54$ Å and $r_{O_4\cdots H} = 1.32$ Å. These lengths are very short compared with typical hydrogen bonds in proteins (44,46) and are considered unrealistic for $Q_A^{\cdot -}$. This indicates that the point-dipole model is inadequate for the case of $Q_A^{\cdot -}$. A more reliable determination of hydrogen-bond lengths is obtained from the ^{2}H nuclear quadrupolar coupling of the deuterated H-bond as discussed in the next section.

H-bond lengths obtained from the quadrupole couplings of ^{2}H

To obtain the hydrogen-bond length from the nqc of ^{2}H, empirical linear relationships were proposed by Soda and Chiba (24) and Hunt and Mackay (25). These are based on a large variety of different hydrogen bonds in chemical and biological systems for which the ^{2}H nqc was determined (mostly by nuclear quadrupole resonance). It should be mentioned that these systems are all diamagnetic, but the addition of an unpaired electron is not expected to significantly change the field gradient and the nqc. We therefore assume that these relationships are also valid for the case of hydrogen bonding to quinone radical anions. This has been corroborated by DFT calculations (28), which showed good agreement with the empirical relations proposed in (24,25). It has been shown (24,25) that the nqc follows a $r^{-3}_{O\cdots D}$ dependence of the form

$$e^2qQ/h = 2P_1 = a - \frac{b}{r^3_{O\cdots D}}[\text{kHz}], \qquad (10)$$

where P_1 is the largest principal component of the nqc tensor, in our case $P_{z''}$ (see Table 1), and a, b are empirical parameters. Their values are given to: $a = 310$ kHz, $b = 572$ kHz · Å^3 (24): $a = 328$ kHz, $b = 643$ kHz · Å^3 (25). We have used this model to determine the lengths of the D-bonds to benzosemiquinone in water and have shown that the value obtained was in agreement with that obtained by other methods (e.g., DFT) (27,28). Using the average of the two sets of values of a and b ($a = 319$ kHz, $b = 607$ kHz · Å^3), and the value of $P_{z''}$ measured for the two D-bonds to $Q_A^{\cdot -}$ (Table 1), we obtain from Eq. 10 bond lengths of

$$r_{O_1\cdots D} = 1.73 \pm 0.03\,\text{Å}\,(\text{Ala M260}), \qquad (11)$$

$$r_{O_4\cdots D} = 1.60 \pm 0.04\,\text{Å}\,(\text{His M219}). \qquad (12)$$

The errors in Eqs. 11 and 12 were obtained considering only the statistical uncertainties of $P_{z''}$ (see Table 1). If the uncertainties of a and b (estimated from the discrepancies obtained in refs. (24) and (25)) are considered the errors increase to 0.05 Å in both cases. The bond length of $N{-}D\cdots O_1$ (Ala M260) is similar to that observed for the benzosemiquinone radical anion in water (1.76 ± 0.03 Å) (27,28), whereas the bond length of $N_\delta{-}D\cdots O_4$ (His M219) is in the range of short hydrogen bonds for biological systems (44,46).

Comparison of the dipolar hyperfine coupling tensor components of ^{1}H and ^{2}H

We determined the D-bond length from the nqc values (Eqs. 11 and 12). To ascertain whether the H-bond length is the same we need to determine whether there is an isotope effect, i.e., whether the bond length changes when ^{1}H is replaced by ^{2}H. This was accomplished by comparing the magnitudes of the dipolar hfc tensor components of ^{1}H and ^{2}H. To compare ^{1}H and ^{2}H dipolar hfc values, the ^{2}H couplings were multiplied by the ratio of their magnetic moments ($\gamma_{1H}/\gamma_{2H} = 6.514$) (see Table 2). The comparison shows that within experimental error the same dipolar hfc tensor components of ^{1}H and ^{2}H (i.e., equal bond lengths) were obtained for Ala M260 (O_1). However, in the case of His M219 (O_4), the observed anisotropic hfc of ^{2}H is ~2% smaller than that of ^{1}H, indicating an isotope effect. This is barely outside the experimental error, but when taken at face-value, would result in a 0.01 Å longer D-bond length as expected for an isotope effect (46). For hydrogen bonds in the solid state with lengths similar to those of the H-bonds to $Q_A^{\cdot -}$ in RCs, isotope effects have been reported to lie between 0 and ~0.02 Å (45). Thus, the magnitude and direction of the observed effect is consistent with an isotope effect for the strong hydrogen bond from His (M219) to $Q_A^{\cdot -}$. However, the putative change in bond length of 0.01 Å is considerably smaller than the uncertainty (see Eq. 12), and therefore Eqs. 11 and 12 are also applicable to the H-bond lengths.

The significance of the isotropic hyperfine interaction

From the hfc tensor analysis a significantly larger isotropic component has been found for the proton hydrogen-bonded to His (M219) compared to Ala (M260) (Table 2). This indicates a partial covalent character of the hydrogen bond to histidine (45,47). This can be explained by a shorter distance and also a larger out-of-plane angle of this H-bond. Both effects lead to a stronger interaction with the electron spin that is located in the π-system of the quinone radical anion. A large isotropic hfc has also been reported for the donor

nitrogen N_δ of His (M219) (12,15). This indicates a flow of spin density via the hydrogen bond to the histidine that is ligated to the metal. This suggests that the hydrogen bonds not only have a structural function in the RC but also play a role in the electron transfer process (15,43).

Effect of the H-bonds on the electronic structure and function of the primary quinone

The full characterization of the geometry of the H-bonds to $Q_A^{\cdot -}$ clearly shows an asymmetrical H-bond situation with the shorter bond, the larger isotropic hfc, and the larger out-of-plane angle corresponding to His (M219). This indicates that the stronger hydrogen bond is to His (M219), which is in agreement with previous interpretations (6,11,14,48–50). The asymmetry of the H-bonds has a profound effect on the spin density distribution of the quinone radical anion that can be rationalized in a simple valence bond model (see, e.g., (6,51)). The consequences are seen in the ^{13}C (11,14,48), ^{17}O (10), and even the ^{1}H hfc values (6,10) of $Q_A^{\cdot -}$ that are shifted when compared with the same ubiquinone radical anion outside the protein—e.g., in organic solvents (4,6, 10,17,51,52). The asymmetric H-bonds and the change of the electronic structure of $Q_A^{\cdot -}$ might have several implications for the function of this quinone in the RC. First, it can be expected that the redox potential is changed; in particular, the second reduction of the quinone is more difficult. This is in agreement with the fact that Q_A in the RC only accepts one electron, i.e., it functions as a one-electron-gate, whereas Q_B, which has more symmetrical H-bonds (6), can be doubly reduced and protonated and forms the hydroquinone. Secondly, it has been shown in this work that the formation of $Q_A^{\cdot -}$ leads to significantly shorter H-bonds as compared to Q_A (see Eqs. 8, 9, 11, and 12), which stabilizes the radical anion. A shorter H-bond is found to the histidine that is liganded to the divalent metal. From the measured isotropic hfc values of the hydrogen-bonded proton and the histidine nitrogen N_δ, a flow of spin density of the transferred electron is evident. It is suggestive that this experimental finding is related to the electron transfer process from $Q_A^{\cdot -}$ to Q_B and also from $Q_A^{\cdot -}$ to $Q_B^{\cdot -}$ via the histidine(s). A possible involvement of the divalent metal is still under discussion (53). In this respect it is worth mentioning that for the biradical state $Q_A^{\cdot -}Q_B^{\cdot -}$ an exchange coupling ($J_o/h = -82$ MHz) has been determined (34,54) that can be related to the electron transfer between the two quinones. A possible pathway for the ET is via the histidine residues. It has been experimentally determined that these histidines carry a small portion of spin density in the respective $Q_A^{\cdot -}$ and $Q_B^{\cdot -}$ states (12,15,16).

SUMMARY AND CONCLUSION

From a fitting of a model spin Hamiltonian to the ENDOR spectra of $Q_A^{\cdot -}$ we were able to characterize the hydrogen bonds to the two carbonyl oxygens of $Q_A^{\cdot -}$ in bacterial reaction centers of *Rb. sphaeroides*. The directions of the hydrogen bonds were obtained from the hyperfine coupling tensors and the bond lengths from the magnitude of the nuclear quadrupolar couplings. An asymmetrical H-bond situation was obtained for $Q_A^{\cdot -}$ with the shorter H-bond to His (M219) ($N_\delta{-}H^{\cdot\cdot}O_4$) and the longer one to Ala (M260) ($N{-}H^{\cdot\cdot}O_1$). The H-bond to the histidine is shorter, better aligned to the $N{-}H^{\cdot\cdot}O$ axis and more out-of-plane with respect to the quinone π-system. This leads to an effective flow of spin density via this H-bond onto the histidine. This aspect may be important for the electron transfer process from $Q_A^{\cdot -}$ to Q_B (or from $Q_A^{\cdot -}$ to $Q_B^{\cdot -}$). It is suggestive that nature might use the H-bonds to fine-tune the geometrical and electronic structure and thereby optimize the ET in the RC.

It is known from studies of the primary donor in RCs that H-bonding can drastically affect the redox potential of a cofactor (55–59). The asymmetric H-bond situation to $Q_A^{\cdot -}$ is known to have a profound effect on the spin density distribution and the electronic structure of the ubiquinone radical anion $Q_A^{\cdot -}$. This may also affect the redox potential of the primary quinone and contribute to the fact that Q_A has the correct potential for the activationless electron transfer from the bacteriopheophytin $\phi_A^{\cdot -}$ to Q_A and functions as a one-electron gate in the ET to Q_B.

The approach described in this work should be applicable to $Q_B^{\cdot -}$ in bacterial RCs, and to the quinones in PSI and PSII of oxygen-evolving organisms. Quinones also play an important role in many other energy-conserving systems, e.g., in the proteins of the respiratory chain (60). In many of these systems stable semiquinone radical intermediates have been detected (e.g., (61)). We believe that the principles described here also apply to these systems.

SUPPLEMENTARY MATERIAL

An online supplement to this article can be found by visiting BJ Online at http://www.biophysj.org.

We thank H. Axelrod (Stanford Synchrotron Radiation Laboratory) for assistance in the use of the program CNS_Solve and for helpful discussions.

This work was supported by National Science Foundation grant No. MCB 99/82186 and National Institutes of Health grant No. GM13191 and by the Max-Planck Society, and Fonds der Chemischen Industrie (to W.L.).

REFERENCES

1. Cramer, W. A., and D. B. Knaff. 1990. *In* Energy Transduction in Biological Membranes. Chapter 5. Springer-Verlag, New York.
2. Ermler, U., G. Fritzsch, S. K. Buchanan, and H. Michel. 1994. Structure of the photosynthetic reaction centre from *Rhodobacter sphaeroides* at 2.65 Å resolution: cofactors and protein-cofactor interactions. *Structure*. 2:925–936.
3. Stowell, M. H. B., T. M. McPhillips, D. C. Rees, S. M. Soltis, E. Abresch, and G. Feher. 1997. Light-induced structural changes in

photosynthetic reaction center: implications for mechanism of electron-proton transfer. *Science*. 276:812–816.

4. Feher, G. 1998. The primary and secondary electron acceptors in bacterial photosynthesis: I. A chronological account of their identification by EPR. *Appl. Magn. Reson.* 15:23–38.
5. Feher, G., and M. Y. Okamura. 1999. The primary and secondary acceptors in bacterial photosynthesis: II. The structure of the Fe^{2+}-$Q^{\cdot -}$ complex. *Appl. Magn. Reson.* 16:63–100.
6. Lubitz, W., and G. Feher. 1999. The primary and secondary acceptors in bacterial photosynthesis: III. Characterization of the quinone radicals $Q_A^{\cdot -}$ and $Q_B^{\cdot -}$ by EPR and ENDOR. *Appl. Magn. Reson.* 17:1–48.
7. Katona, G., U. Andreasson, E. M. Landau, L. E. Andreasson, and R. Neutze. 2003. Lipidic cubic phase crystal structure of the photosynthetic reaction centre from *Rhodobacter sphaeroides* at 2.35 Å resolution. *J. Mol. Biol.* 331:681–692.
8. Abresch, E. C., A. P. Yeh, S. M. Soltis, D. C. Rees, H. L. Axelrod, M. Y. Okamura, and G. Feher. 1999. Crystal structure of the charge-separated state, $D^{\cdot +}Q_A^{\cdot -}$, in photosynthetic reaction centers from *Rb. sphaeroides*. *Biophys. J.* 76:A141. (Abstr.).
9. Lubitz, W., E. C. Abresch, R. J. Debus, R. A. Isaacson, M. Y. Okamura, and G. Feher. 1985. Electron nuclear double resonance of semiquinones in reaction centers of *Rhodopseudomonas sphaeroides*. *Biochim. Biophys. Acta.* 808:464–469.
10. Feher, G., R. A. Isaacson, M. Y. Okamura, and W. Lubitz. 1985. ENDOR of semiquinones in RCs from *Rhodopseudomonas sphaeroides*. *In* Antennas and Reaction Centers of Photosynthetic Bacteria—Structure, Interactions and Dynamics. M. E. Michel-Beyerle, editor. Springer-Verlag, Berlin.
11. van den Brink, J. S., A. P. Spoyalov, P. Gast, W. B. S. van Liemt, J. Raap, J. Lugtenburg, and A. J. Hoff. 1994. Asymmetric binding of the primary acceptor quinone in reaction centers of the photosynthetic bacterium *Rhodobacter sphaeroides* R26, probed with Q-band (35 GHz) EPR spectroscopy. *FEBS Lett.* 353:273–276.
12. Bosch, M. K., P. Gast, A. J. Hoff, A. P. Spoyalov, and Y. D. Tsvetkov. 1995. The primary acceptor quinone Q_A in reaction centers of *Rhodobacter sphaeroides* R26 is hydrogen-bonded to the $N^{\delta(1)}$–H of His M219. An electron spin echo study of $Q_A^{\cdot -}$. *Chem. Phys. Lett.* 239:306–312.
13. Isaacson, R. A., F. Lendzian, E. C. Abresch, W. Lubitz, and G. Feher. 1995. Electronic structure of $Q_A^{\cdot -}$ in reaction centers from *Rhodobacter sphaeroides*. I. Electron paramagnetic resonance in single crystals. *Biophys. J.* 69:311–322.
14. Isaacson, R. A., E. C. Abresch, F. Lendzian, C. Boullais, M. L. Paddock, C. Mioskowski, W. Lubitz, and G. Feher. 1996. Asymmetry of the binding sites of $Q_A^{\cdot -}$ and $Q_B^{\cdot -}$ in reaction centers of *Rb. sphaeroides* probed by Q-band EPR with ^{13}C-labeled quinones. *In* The Reaction Center of Photosynthetic Bacteria: Structure and Dynamics. M. B. Michel-Beyerle, editor. Springer-Verlag, Berlin.
15. Lendzian, F., J. Rautter, H. Kass, A. Gardiner, and W. Lubitz. 1996. ENDOR and pulsed EPR studies of photosynthetic reaction centers: protein-cofactor interactions. *Ber. Bunsen. Phys. Chem.* 100:2036–2040.
16. Spoyalov, A. P., R. J. Hulsebosch, S. Shochat, P. Gast, and A. J. Hoff. 1996. Evidence that Ala M260 is hydrogen-bonded to the reduced primary acceptor quinone $Q_A^{\cdot -}$ in reaction centers of *Rb. sphaeroides*. *Chem. Phys. Lett.* 263:715–720.
17. Rohrer, M., F. MacMillan, T. F. Prisner, A. T. Gardiner, K. Mobius, and W. Lubitz. 1998. Pulsed ENDOR at 95 GHz on the primary acceptor ubisemiquinone $Q_A^{\cdot -}$ in photosynthetic bacterial reaction centers and related model systems. *J. Phys. Chem. B.* 102:4648–4657.
18. Paddock, M. L., E. C. Abresch, R. A. Isaacson, W. Lubitz, M. Y. Okamura, and G. Feher. 1999. Identification of hydrogen bonds to $Q_A^{\cdot -}$ in RCs of *Rb. sphaeroides* by ENDOR spectroscopy. *Biophys. J.* 76:A141. (Abstr.).
19. Flores, M., R. Isaacson, E. Abresch, R. Calvo, W. Lubitz, and G. Feher. 2006. Protein-cofactor interactions in bacterial reaction centers from *Rhodobacter sphaeroides* R-26: I. Identification of the ENDOR lines associated with the hydrogen bonds to the primary quinone $Q_A^{\cdot -}$. *Biophys. J.* 90:3356–3362.
20. Debus, R. J., G. Feher, and M. Y. Okamura. 1986. Iron-depleted reaction centers from *Rhodopseudomonas sphaeroides* R-26.1: characterization and reconstitution with Fe^{2+}, Mn^{2+}, Co^{2+}, Ni^{2+}, Cu^{2+}, and Zn^{2+}. *Biochemistry.* 25:2276–2287.
21. Utschig, L. M., S. R. Greenfield, J. Tang, P. D. Laible, and M. C. Thurnauer. 1997. Influence of iron-removal procedures on sequential electron transfer in photosynthetic bacterial reaction centers studied by transient EPR spectroscopy. *Biochemistry.* 36:8548–8558.
22. Rist, G. H., and J. S. Hyde. 1968. Ligand ENDOR of Cu-8-hydroxyquinolinate substituted into a single crystal and a powder of phthalimide. *J. Chem. Phys.* 49:2449–2451.
23. Stoll, S., and A. Schweiger. 2006. EasySpin, a comprehensive software package for spectral simulation and analysis in EPR. *J. Magn. Reson.* 178:42–55.
24. Soda, G., and T. Chiba. 1969. Deuteron magnetic resonance study of cupric sulfate pentahydrate. *J. Chem. Phys.* 50:439–455.
25. Hunt, M. J., and A. L. Mackay. 1974. Deuterium and nitrogen pure quadrupole resonance in deuterated amino acids. *J. Magn. Reson.* 15:402–414.
26. Weil, J. A., J. R. Bolton, and J. E. Wertz. 1994. Electron Paramagnetic Resonance. Elementary Theory and Practical Applications. Wiley, New York.
27. Flores, M., R. A. Isaacson, R. Calvo, G. Feher, and W. Lubitz. 2003. Probing hydrogen bonding to quinone anion radicals by ^1H and ^2H ENDOR spectroscopy at 35 GHz. *Chem. Phys.* 294:401–413.
28. Sinnecker, S., E. Reijerse, F. Neese, and W. Lubitz. 2004. Hydrogen bond geometries from electron paramagnetic resonance and electron-nuclear double resonance parameters: density functional study of quinone radical anion-solvent interactions. *J. Am. Chem. Soc.* 126: 3280–3290.
29. Blinc, R. 1976. Magnetic resonance studies of hydrogen bonding in solids. *In* The Hydrogen Bond; Recent Developments in Theory and Experiments. II. Structure and Spectroscopy. P. Schuster, G. Zundel, and C. Sandorfy, editors. North-Holland, Amsterdam.
30. Soda, G., and T. Chiba. 1969. Deuteron magnetic resonance study of cupric formate tetrahydrate $Cu(DCOO)_2.4D_2O$. *J. Phys. Soc. Jpn.* 26:249–261.
31. Schweiger, A., and G. Jeschke. 2001. Principles of Pulse Electron Paramagnetic Resonance. Oxford University Press, Oxford.
32. Hoffman, B. M., V. J. DeRose, P. E. Doan, R. J. Gurbiel, A. L. P. Houseman, and J. Telser. 1993. Metalloenzyme active-site structure and function through multifrequency CW and pulsed ENDOR. *In* Biological Magnetic Resonance, Vol. 13. Chapter 5. L. Berliner and J. Reuben, editors. Plenum Press, New York.
33. Hüttermann, J. 1993. ENDOR of randomly oriented mononuclear metalloproteins: toward structural determinations of the prosthetic group. *In* Biological Magnetic Resonance, Vol. 13. Chapter 5. L. Berliner and J. Reuben, editors. Plenum Press, New York.
34. Calvo, R., E. C. Abresch, R. Bittl, G. Feher, W. Hofbauer, R. A. Isaacson, W. Lubitz, M. Y. Okamura, and M. L. Paddock. 2000. EPR study of the molecular and electronic structure of the semiquinone biradical $Q_A^{\cdot -}Q_B^{\cdot -}$ in photosynthetic reaction centers from *Rhodobacter sphaeroides*. *J. Am. Chem. Soc.* 122:7327–7341.
35. Kirkpatrick, S., C. D. Gelatt, and M. P. Vecchi. 1983. Optimization by thermal annealing. *Science.* 220:671–680.
36. Burghaus, O., M. Plato, M. Rohrer, K. Mobius, F. MacMillan, and W. Lubitz. 1993. Three-mm high-field EPR on semiquinone radical anions $Q^{\cdot -}$ related to photosynthesis and on the primary donor $P^{\cdot +}$ and acceptor $Q_A^{\cdot -}$ in reaction centers of *Rhodobacter sphaeroides* R-26. *J. Phys. Chem. B.* 97:7639–7647.
37. O'Malley, P. J. 2001. Electronic structure studies of quinone and semiquinones: accurate calculation of spin densities and electron paramagnetic resonance parameters. *Antioxid. Redox. Sign.* 3:825–838.
38. Lucken, E. A. C. 1969. Nuclear Quadrupole Couplings Constants. Academic Press, London, New York.
39. Mayas, L., M. Plato, C. J. Winscom, and K. Mobius. 1978. Deuterium quadrupole coupling constants in hydrogen bonded dicarboxylic acids. A distant ENDOR study. *Mol. Phys.* 36:753–764.

40. Brunger, A. T., P. D. Adams, G. M. Clore, W. L. DeLano, P. Gros, R. W. Grosse-Kunstleve, J. Jiang, J. Kuszewski, M. Nilges, N. S. Pannu, R. J. Read, L. M. Rice, T. Simonson, and G. L. Warren. 1998. Crystallography and NMR system: a new software suite for macromolecular structure determination. *Acta Crystallogr. D.* 54:905–921.

41. Axelrod, H. L., E. C. Abresch, M. L. Paddock, M. Y. Okamura, and G. Feher. 2000. Determination of the binding sites of the proton transfer inhibitors Cd^{2+} and Zn^{2+} in bacterial reaction centers. *Proc. Natl. Acad. Sci. USA.* 97:1542–1547.

42. Axelrod, H. L., E. C. Abresch, M. Y. Okamura, A. P. Yeh, D. C. Rees, and G. Feher. 2002. X-ray structure determination of the cytochrome c_2: reaction center electron transfer complex from *Rhodobacter sphaeroides*. *J. Mol. Biol.* 319:501–515.

43. Sinnecker, S., M. Flores, and W. Lubitz. 2006. Protein-cofactor interactions in bacterial reaction centers from *Rhodobacter sphaeroides* R-26: effect of hydrogen bonding on the electronic and geometric structure of the primary quinone. A density functional theory study. *Phys. Chem. Chem. Phys.* 8:5659–5670.

44. Jeffrey, G. A. 1997. An Introduction to Hydrogen Bonding. Oxford University Press, Oxford.

45. Steiner, T. 2002. The hydrogen bond in the solid state. *Angew. Chem. Int. Ed. Engl.* 41:48–76.

46. Jeffrey, G. A., and W. Saenger. 1991. Hydrogen Bonding in Biological Structures. Springer-Verlag, Berlin.

47. Gilli, P., V. Bertolasi, V. Ferretti, and G. Gilli. 1994. Covalent nature of the strong homonuclear hydrogen bond. Study of the O−H−O system by crystal structure correlation methods. *J. Am. Chem. Soc.* 116:909–915.

48. Hoff, A. J., T. N. Kropacheva, R. I. Samoilova, N. P. Gritzan, J. Raap, J. S. van den Brink, P. Gast, and J. Lugtenburg. 1996. Site-directed isotope labelling as a tool in spectroscopy of photosynthetic preparations. Investigations on quinone binding in bacterial reaction centers. *In* The Reaction Center of Photosynthetic Bacteria: Structure and Dynamics. M. B. Michel-Beyerle, editor. Springer-Verlag, Berlin.

49. Breton, J., C. Boullais, J. R. Burie, E. Nabedryk, and C. Mioskowski. 1994. Binding sites of quinones in photosynthetic bacterial reaction centers investigated by light-induced FTIR difference spectroscopy: assignment of the interactions of each carbonyl of Q_A in *Rhodobacter sphaeroides* using site-specific ^{13}C-labeled ubiquinone. *Biochemistry.* 33:14378–14386.

50. Brudler, R., H. J. M. de Groot, W. B. S. van Liemt, W. F. Steggerda, R. Esmeijer, P. Gast, A. J. Hoff, J. Lugtenburg, and K. Gerwert. 1994. Asymmetric binding of the 1- and 4-C=O groups of Q_A in *Rhodobacter sphaeroides* R26 reaction centres monitored by Fourier transform infra-red spectroscopy using site-specific isotopically labelled ubiquinone-10. *EMBO J.* 13:5523–5530.

51. MacMillan, F., F. Lendzian, and W. Lubitz. 1995. EPR and ENDOR characterization of semiquinone anion radicals related to photosynthesis. *Magn. Reson. Chem.* 33:S81–S93.

52. Das, M. R., H. D. Conner, D. S. Leniart, and J. H. Freed. 1970. An electron nuclear double resonance and electron spin resonance study of semiquinones related to vitamins K and E. *J. Am. Chem. Soc.* 92:2258–2268.

53. Remy, A., and K. Gerwert. 2003. Coupling of light-induced electron transfer to proton uptake in photosynthesis. *Nat. Struct. Biol.* 10:637–644.

54. Calvo, R., R. A. Isaacson, M. L. Paddock, E. C. Abresch, M. Y. Okamura, A. L. Maniero, L. C. Brunel, and G. Feher. 2001. EPR study of the semiquinone biradical $Q_A^{-}Q_B^{-}$ in photosynthetic reaction centers of *Rhodobacter sphaeroides* at 326 GHz: determination of the exchange interaction J_o. *J. Phys. Chem. B.* 105:4053–4057.

55. Allen, J. P., and J. C. Williams. 1995. Relationship between the oxidation potential of the bacteriochlorophyll dimer and electron transfer in photosynthetic reaction centers. *J. Bioenerg. Biomembr.* 27:275–283.

56. Rautter, J., F. Lendzian, C. Schulz, A. Fetsch, M. Kuhn, X. Lin, J. C. Williams, J. P. Allen, and W. Lubitz. 1995. ENDOR studies of the primary donor cation radical in mutant reaction centers of *Rhodobacter sphaeroides* with altered hydrogen-bond interactions. *Biochemistry.* 34:8130–8143.

57. Muh, F., F. Lendzian, M. Roy, J. C. Williams, J. P. Allen, and W. Lubitz. 2002. Pigment-protein interactions in bacterial reaction centers and their influence on oxidation potential and spin density distribution of the primary donor. *J. Phys. Chem. B.* 106:3226–3236.

58. Lubitz, W., F. Lendzian, and R. Bittl. 2002. Radicals, radical pairs and triplet states in photosynthesis. *Acc. Chem. Res.* 35:313–320.

59. Kalman, L., R. LoBrutto, J. P. Allen, and J. C. Williams. 1999. Modified reaction centres oxidize tyrosine in reactions that mirror photosystem II. *Nature.* 402:696–699.

60. Berg, J. M., J. L. Tymoczko, and L. Stryer. 2002. Biochemistry. W. H. Freeman, New York.

61. Grimaldi, S., F. MacMillan, T. Ostermann, B. Ludwig, H. Michel, and T. Prisner. 2001. $Q_H^{\cdot-}$ ubisemiquinone radical in the bo_3-type ubiquinol oxidase studied by pulsed electron paramagnetic resonance and hyperfine sublevel correlation spectroscopy. *Biochemistry.* 40:1037–1043.